AGU ADVANCING EARTH AND SPACE SCIENCE

JGR Solid Earth

RESEARCH ARTICLE

10.1029/2020JB020925

Key Points:

- The noise content of underwater distributed acoustic sensing (DAS) along three different telecommunication cables is quantified and compared to adjacent broadband stations
- Earthquake detection capabilities using DAS are similar to those of broadband instruments
- Detection capabilities are mainly a function of the recorded noise, cable response, and apparent velocity

Supporting Information:

- Supporting Information S1

Correspondence to:

I. Lior,
itzhaklior22@gmail.com

Citation:

Lior, I., Sladen, A., Rivet, D., Ampuero, J.-P., Hello, Y., Becerril, C., et al. (2021). On the detection capabilities of underwater distributed acoustic sensing. *Journal of Geophysical Research: Solid Earth*, *126*, e2020JB020925. https://doi.org/10.1029/2020JB020925

Received 3 SEP 2020
Accepted 28 JAN 2021

On the Detection Capabilities of Underwater Distributed Acoustic Sensing

Itzhak Lior[1], Anthony Sladen[1], Diane Rivet[1], Jean-Paul Ampuero[1], Yann Hello[1], Carlos Becerril[1,2], Hugo F. Martins[3], Patrick Lamare[4], Camille Jestin[5], Stavroula Tsagkli[6], and Christos Markou[6]

[1]Université Côte d'Azur, CNRS, Observatoire de la Côte d'Azur, IRD, Géoazur, [2]Department of Electronics, University of Alcalá, Alcalá de Henares, Spain, [3]Instituto de Óptica, CSIC, Madrid, Spain, [4]Aix Marseille University, CNRS/IN2P3, CPPM, Marseille, France, [5]Febus Optics, Pau, France, [6]NCSR Demokritos, Institute of Nuclear and Particle Physics, Ag. Paraskevi Attikis, Athens, Greece

Abstract The novel technique of distributed acoustic sensing (DAS) holds great potential for underwater seismology by transforming standard telecommunication cables, such as those currently traversing various regions of the world's oceans, into dense arrays of seismo-acoustic sensors. To harness these measurements for seismic monitoring, the ability to record transient ground deformations is investigated by analyzing ambient noise, earthquakes, and their associated phase velocities, on DAS records from three dark fibers in the Mediterranean Sea. Recording quality varies dramatically along the fibers and is strongly correlated with the bathymetry and the apparent phase velocities of recorded waves. Apparent velocities are determined for several well-recorded earthquakes and used to convert DAS S-wave strain spectra to ground motion spectra. Excellent agreement is found between the spectra of nearby underwater and on-land seismometers and DAS converted spectra, when the latter are corrected for site effects. Apparent velocities greatly affect the ability to detect seismic deformations: for the same ground motions, slower waves induce higher strains and thus are more favorably detected than fast waves. The effect of apparent velocity on the ability to detect seismic phases, quantified by expected signal-to-noise ratios, is investigated by comparing signal amplitudes predicted by an earthquake model to recorded noise levels. DAS detection capabilities on underwater fibers are found to be similar to those of nearby broadband sensors, and superior to those of on-land fiber segments, owing to lower velocities at the ocean-bottom. The results demonstrate the great potential of underwater DAS for seismic monitoring and earthquake early warning.

1. Introduction

To date, most observational earthquake research relies on ground motions recorded by seismometers. These instruments are typically installed in proximity to active faults, as the most valuable observations are those obtained very close to earthquake epicenters: they provide the most coherent view of source processes and allow for early detection of large earthquakes and monitoring of small ones. However, there is a severe observational gap: the vast majority of seismometers are located on-land, while the largest earthquakes, and most tsunami generating earthquakes, occur underwater. Existing technologies to overcome this observational gap, e.g., ocean-bottom seismometers (OBS), are very costly and thus not widely implemented. The lacking ocean-bottom monitoring hinders the ability to conduct underwater seismological research. This is especially critical for hazard mitigation tasks such as providing earthquake early warning (EEW) (e.g., Allen & Melgar, 2019; Lior & Ziv, 2020; Vallée et al., 2017) for underwater earthquakes, since precious time is lost waiting for seismic signals to reach on-land stations. Filling this underwater observational gap will greatly benefit hazard mitigation capabilities and constitute a major step forward in seismological research.

In recent years, the innovative approach of distributed acoustic sensing (DAS) is being used for many seismological tasks (Zhan, 2019, and reference therein). This novel array based seismic measurement technique produces strain (or strain-rate) measurements every few meters along tens-of-kilometers long fibers. Since DAS is mostly sensitive to deformation along optical fibers, i.e., extension and compression (e.g., Ajo-Franklin et al., 2019; Kuvshinov, 2016; Mateeva et al., 2014; Papp et al., 2017; Yu et al., 2018), only single component measurements are obtained, oriented along the fiber. Previous studies demonstrate the broadband response of DAS by comparing DAS and co-located broadband seismometers (Jousset et al., 2018; Lindsey et al., 2020; Paitz et al., 2020). These studies show that reliable deformation measurements can be obtained for both low (e.g., ambient noise, large earthquakes) and high (e.g., active sources, small earthquakes) frequency signals.

DAS enables the measurement of transient ground deformations along standard optical fibers such as those inside the telecommunication cables currently traversing various regions of the world's oceans. Implementing DAS technology on available underwater fibers has great potential to fill the underwater observational gap. The ability to record and analyze earthquakes using underwater DAS has been recently demonstrated (Lindsey et al., 2019; Sladen et al., 2019; Williams et al., 2019), but is yet to be fully realized. To reliably harness this technique for earthquake monitoring, the nature of underwater DAS measurements needs to be better understood.

In a previous study, Sladen et al. (2019) used an underwater optical fiber offshore Toulon, South of France, and showed that uneven cable-ground coupling and water-Earth interactions significantly affect the sensitivity to ground motions thus limiting the reliability of earthquake monitoring on underwater telecommunication fibers. Because these underwater cables were installed for the sole purpose of power and data transmission between two points in space, the mechanical coupling between the cable and the ocean-bottom is not uniform along the fiber. This reduces the cable's recording quality to a point that the coupling of several cable segments is insufficient for seismic measurements. The studies by Lindsey et al. (2019) and Willams et al. (2019) relied on seafloor buried cables, which reduced many of these problems. Cable sections deployed at shallow depths are frequently buried to avoid fishing/trawling or prevent damage to biological systems. However, such buried segments are just a small fraction of the global network of seafloor cables. Sladen et al. (2019) also found that underwater DAS earthquake recordings are dominated by Scholte-waves, indicating that acoustic and seismic waves are converted and scattered at the ocean—solid-earth interface. Moreover, interactions between the water-column and solid-earth generate several noise sources, i.e., surface gravity waves and microseisms, which constitute coherent noise that could affect earthquake monitoring with underwater DAS measurements.

Fully unlocking the potential of underwater DAS will facilitate the use of optical fibers as next-generation dense seismic networks, overcoming the disadvantages of discrete, mainly on-land, seismic sensors, thus filling a vast observational gap. A significant first step, is to understand and quantify earthquake detection and measurement abilities and set detection thresholds by characterizing measured noise, seismic signals, and their relation to ground motions. To this end, underwater DAS noise and seismic signals are analyzed here using data recorded by three different underwater DAS fiber cables, one in France and two in Greece. DAS records are then compared to those of nearby broadband stations, two of which are located underwater.

This manuscript is organized as follows. In the next section, the data set used for this study is described. Then, underwater DAS noise is characterized by computing noise power spectral densities (PSDs). In Section 4, several cataloged earthquakes are used to analyze the response of the different fibers to ground deformation and the conversion from DAS recorded strain to ground motions. Finally, implications for DAS detection capabilities are discussed.

2. Data

This study uses a data set of underwater DAS records, acquired by Géoazur, from three underwater cables: two offshore Methoni, south-west Greece, and one offshore Toulon, South of France. In addition, data from four on-land and two underwater broadband stations, installed near the cables, are used. The cables' locations, depth profiles, and broadband station locations are shown in Figure 1. Because these cables were simply deployed to provide communication between the two ends of the fiber, the cables' exact geographical position and bathymetric profiles are not well constrained. Cable locations are interpolated from the deploying ships' trajectories, and bathymetric profiles along these paths are obtained using available bathymetry maps. Several shallow cable segments are artificially buried, as further detailed, yet are subject to natural sediment mobilization by currents, storms or other ocean-

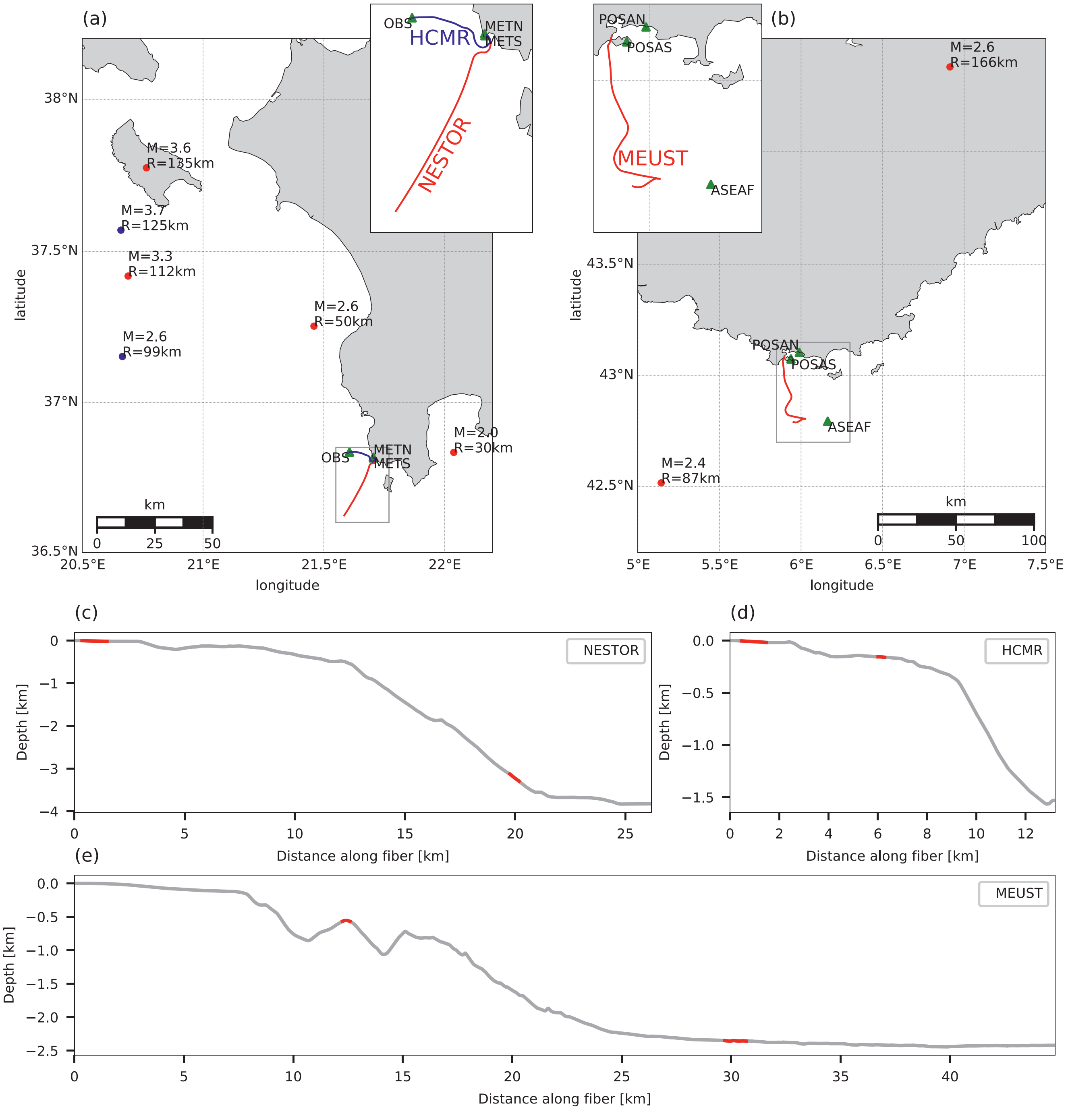

Figure 1. Maps of Methoni and Toulon regions along with cable depth profiles. Map of the (a) Methoni and (b) Toulon regions along with cable locations, broadband stations, and analyzed earthquakes. The Hellenic Center for Marine Research (HCMR), Neutrino Extended Submarine Telescope with Oceanographic Research (NESTOR), and Mediterranean Eurocentre for Underwater Sciences and Technologies (MEUST) cables, along with their recorded earthquakes, are indicated in blue and red (left panel), and red (right panel), respectively. Insets correspond to regions marked by gray rectangles. Depth profiles along the cables' trajectories are shown in panels (c–e) starting at the on-land end of each cable (interrogator location) and ending at the ocean bottom end. Sections used in subsequent analysis are indicated in red.

ographic effects that may expose previously buried segments and bury exposed sections. All cables recorded several local earthquakes during the measurement campaigns; those analyzed in the next sections are indicated in Figure 1 and listed in Table 1. Here, the cables and instrumental setup are described.

Table 1
Earthquakes Used in This Study

Cable name	Origin time (UTC)	Magnitude (local)	Location (latitude, longitude, depth [km])	Catalog
NESTOR	22/04/2019 19:26:06	3.3	37.4185, 20.6897, 11.0	Athens University
	23/04/2019 17:29:40	3.6	37.7753, 20.7658, 7.0	Athens University
	21/04/2019 22:11:47	2.0	36.8335, 22.0382, 2.0	Athens University
	23/04/2019 19:25:51	2.6	37.2528, 21.4593, 9.0	Athens University
HCMR	18/04/2019 21:44:42	3.7	37.57, 20.66, 8.0	EMSC
	19/04/2019 03:30:19	2.6	37.1523, 20.6662, 1.0	Athens University
MEUST	19/07/2019 21:16:57	2.6	44.374, 6.913, 2.6	Géoazur
	21/07/2019 23:01:58	2.4	42.516, 5.143, 2.0	Géoazur

DAS data from Greece were acquired on two adjacent dark optical fibers, situated on the central Hellenic shear zone, near a triple junction: the Kephalonia Transform Fault to the north-west, and the Hellenic Trench and Mediterranean Ridge to the south-east (Finetti, 1982). These cables are intended for the HCMR (Hellenic Center for Marine Research) and NESTOR (Neutrino Extended Submarine Telescope with Oceanographic Research) (Aggouras et al., 2005; Anassontzis & Koske, 2003) projects. DAS data were acquired on April 18 and 19, 2019 on the HCMR cable and from April 19 to 25 on the NESTOR cable. The HCMR and NESTOR cables span 13.2 and 26.2 km, respectively: from a common landing point, they follow the same path for the first kilometer (at different conduits) inside the shallow Methoni Bay, and then diverge in different directions toward the bottom of the East Ionian Sea (Figure 1). The NESTOR cable was deployed with 3% slack and consists of a heavy armor (HA) part for the first 12.5 km, and a light armor (LA) part until the ocean-bottom end. The former is required owing to the steep and rocky bathymetry. The cable is buried for the first 2 km, inside Methoni Bay, in a depth of ∼1 m. The HCMR cable was deployed with 2% slack and is a single armored (SA) cable. It is buried for the first 1.8 km, inside Methoni Bay, and again from 3.8 to 6.3 km, in a depth of 0.5–1.5 m. These cables were interrogated using an old generation Febus A1-R DAS interrogator, developed by Febus Optics. This single-pulse phase-based system produces longitudinal strain-rate measurement. The optical dephasing between two positions on the optical fiber at gauge length distance is directly linked with longitudinal perturbations applied to the fiber. Raw DAS data was acquired with the following parameter tuning: pulse width was set to 5 m, spatial resolution was set to 3.2 m, amplified power was set to 33 and 30 dBm for HCMR and NESTOR, respectively, and pulse rate frequency was set to 500 Hz for HCMR, and 1,400 and 1,000 Hz for the first 2 and last 4 days for NESTOR, respectively. Raw data was then processed using gauge length and spatial sampling of 19.2 m for both cables, equivalent to 688 and 1,365 channels of strain-rate equally spaced along the HCMR and NESTOR cables, respectively. Strain-rate was computed at intervals of 6 ms for HCMR and 5 ms for NESTOR, producing 68 and 740 GB of data for HCMR and NESTOR, respectively. In addition to DAS data, several broadband seismometers were available during these DAS measurements: two on-land CMG40 sensors, deployed near the interrogator for the duration of the measurements, and one permanent OBS near the end of the HCMR cable. Calibration information for the latter, a Guralp CMG40T, was unavailable. The flat frequency response of this sensor, between 30 s and 50 Hz, includes the recorded seismic signals, thus, a simple empirical response was estimated by comparing available earthquake records between the OBS and the on-land sensors.

The offshore Toulon data were acquired on the same fiber used by Sladen et al. (2019), between July 11 and 31, 2019. The path of this fiber was slightly modified in October 2018, after a first DAS acquisition done by Sladen et al. (2019) (Figure 1). This cable is located in an area of moderate seismicity and is used for the MEUST-NUMerEnv project (Mediterranean Eurocentre for Underwater Sciences and Technologies—Neutrino Mer Environnement) (Lamare, 2016). The cable spans 44.8 km: from the coast to the deep Mediterranean plain and is buried for the first 500 m. The fiber is installed on-land, mostly under a motorway, for the first 1.6 km, then in a double armoring heavy (DAH) for the next 2.1 km, a single armoring heavy (SAH) for the next 15.1 km, and then light weight screened (LWS) until its ocean-bottom end. For this cable, a chirped-pulse hDAS interrogator (high-fidelity distributed acoustic sensor), developed by Aragon Photonics, was used along with Raman amplification (Fernandez-Ruiz et al., 2019; Pastor-Graells et al., 2016; Williams et al., 2019), which produces strain measurements. This system sends linearly chirped-pulses along the fiber and detects minute changes in the pulse's central wavelength when the fiber is perturbed. These slight wavelength changes with time are mapped to strain or temperature changes at specific locations along the fiber. The optical pulses had 100 ns width (10 m optical spatial resolution), 1 GHz spectral content, 50 mW peak power, and the gauge length and spatial sampling were set to 10 m, equivalent to 4,480 equally spaced channels of strain measured along the cable. Distributed Raman amplification with a pump power of 300 mW was used, ensuring an instrumental noise floor variation of <5 dB across the full length of the fiber. The pulse repetition rate was 500 Hz and sampling intervals were set to 10 and 2 ms for the first and last 10 days of the campaign (data downsampling, no optical averaging was used), respectively, producing 16 TB of data. The instrumental strain noise floor was observed to be <100picostrain/sqrt (Hz) along the entire fiber length, matching optimal laboratory measurements of the technology for long fibers (Fernández-Ruiz et al., 2019). In addition, two on-land CMG3-ESP (120 s—80 Hz) sensors, installed near the interrogator, were used. The OBS near the end of the fiber (ASEAF station, CMG3-T) was inactive during this measurement campaign, but OBS records from July 2017 were used for noise analysis. These were obtained at a similar time of year, and represent equivalent water temperature (23°C–24°C) and wave height conditions, as obtained from the Coriolis database (coriolis.eu.org). Ocean-bottom noise recorded at different times may differ due to compliance and tilting effect (e.g., Webb & Crawford, 2010), thus ASEAF noise measurements may not be fully representative of the conditions during the DAS measurement campaign.

3. DAS Noise Analysis

The recorded DAS noise arises from several natural sources, including ocean-solid earth interactions, which produce surface gravity waves and microseisms, which are recorded at frequencies where DAS response is flat (e.g., Lindsey et al., 2020; Paitz et al., 2020). The natural noise amplitude can be affected by local seismic amplification effects. In addition, ground-cable coupling variations modulate the recorded noise and signals, and instrumental noise dominates several frequency-bands along the fibers. In this section, underwater DAS noise is analyzed and quantified.

The noise content of underwater DAS records and broadband sensors is quantified by computing PSDs. These PSDs were calculated for the full duration of each campaign at every measurement point along the fibers (Peterson, 1993). To this end, we closely follow the PSD calculation procedure described in McNamara and Buland (2004). PSDs for the OBS at the end of the HCMR cable were not computed due to missing instrumental response. Because seismic noise PSDs are typically obtained for ground motion accelerations (McNamara & Buland, 2004), here they are calculated for strain-rate; the relationship between acceleration and strain-rate, though not straightforward (Section 4.2), facilitates a comparison between both measures. While HCMR and NESTOR records were acquired in strain-rate, MEUST strain records were differentiated to strain-rate in the frequency domain. For each virtual sensor along each fiber (at gauge length spacing), PSDs were calculated for the available records at one-hour intervals. These 1-h PSDs were averaged at each virtual sensor and are plotted in Figure 2 as functions of frequency and distance from the interrogator along the fiber. PSDs for selected locations along the cables, as well as for the broadband sensors, are plotted in Figure 3. The various noise sources shown in Figures 2 and 3 are further described.

Solid-earth—ocean-bottom interactions generate several noise sources, recorded by the fibers. At shallow water depths, DAS records are dominated by surface gravity waves at frequencies of 0.05–0.3 Hz (black curves in Figure 2 and panels a and c of Figure 3). These waves induce primary microseisms when gravity-waves interfere with ocean-bottom topography, which are frequently measured by on-land seismic stations. The dominant frequency of these waves decreases with increasing water depth (red curves in Figure 2) as predicted by the dispersion relation of surface gravity waves. This effect is also seen in the comparison of HCMR and NESTOR PSDs at 1 and 2 km depths (Figure 3a). Surface gravity wave amplitudes are in close

10.1029/2020JB020925

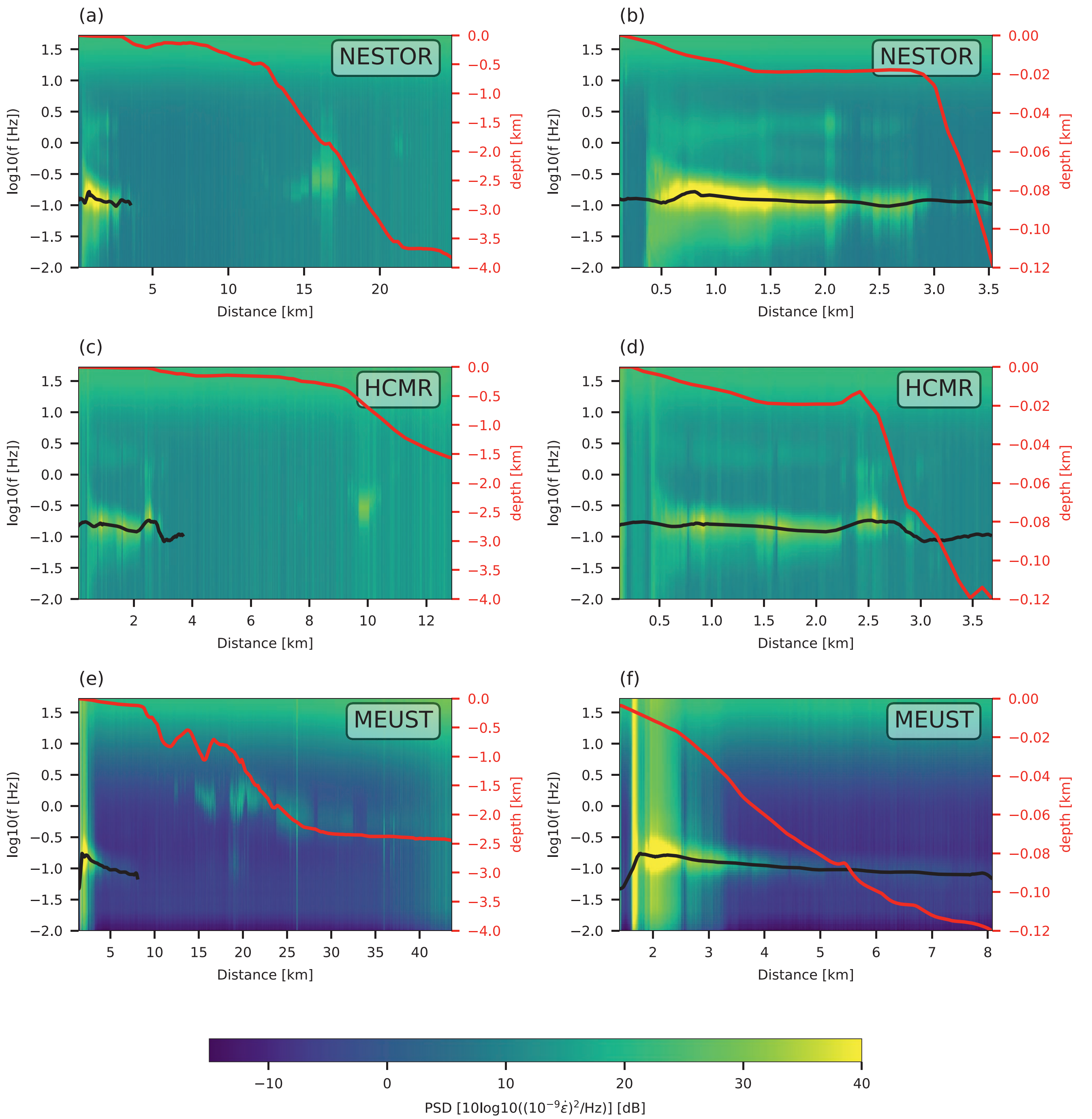

Figure 2. Noise analysis for the three cables: average nano-strain-rate power spectral density (PSD) as a function of frequency and distance along the fibers. Left panels show the full cable and right panels show the cable up to a water depth of 120 m. Red line indicates bathymetric profiles (right axis), and black lines indicate the peak frequency of surface gravity waves (frequency associated with the maximum PSD).

agreement for NESTOR and MEUST in-spite of the different regions and interrogators (panels b and f of Figure 2 and panels a and c of Figure 3), while those recorded by HCMR are slightly lower. The disparity between gravity wave amplitudes obtained by NESTOR and HCMR, both recorded in Methoni Bay, as well as the variability in single one-hour PSDs (thin red and green curves in panel a of Figure 3), indicate that they are affected by local meteorological conditions: during the NESTOR measurements a storm occurred, inducing higher amplitude gravity waves.

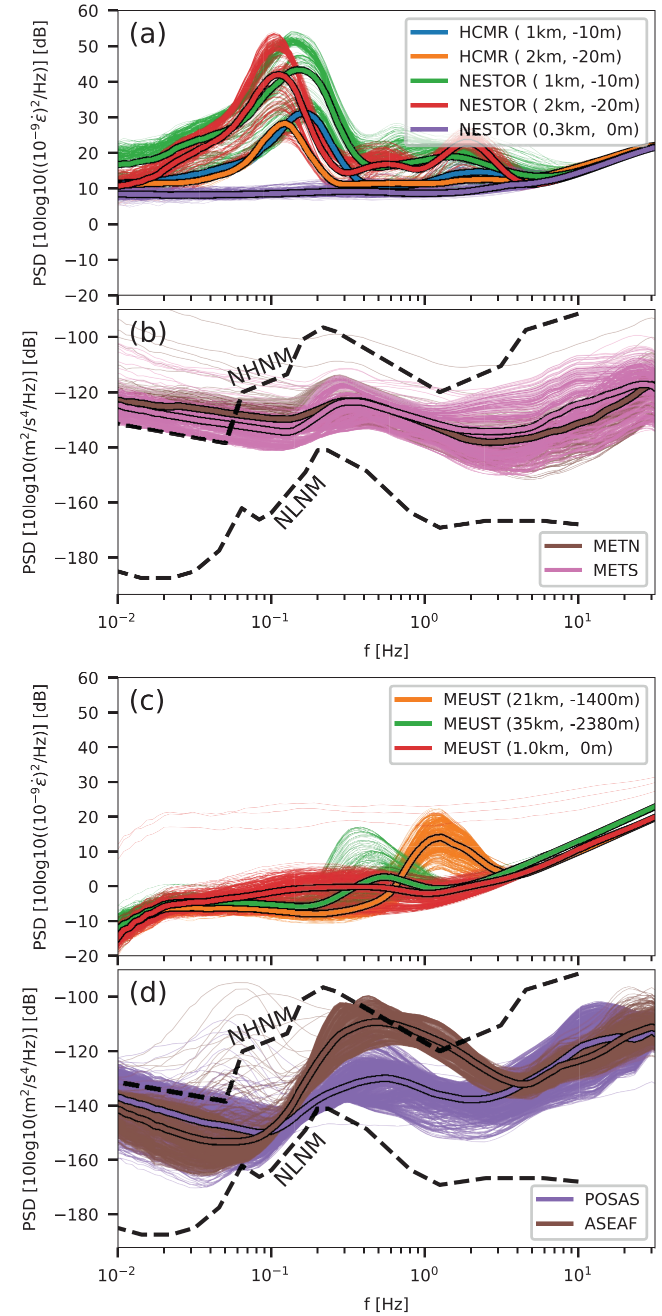

Figure 3. Comparison of distributed acoustic sensing (DAS) nano strain-rate (panels a and c) and broadband acceleration (panels b and d) PSD. DAS PSDs are displayed for specific distances from the interrogator and water depths as indicated in the panel legends. NESTOR PSD at 0.3 km (purple curve in a) and MEUST PSD at 1 km (red curve in c) correspond to on-land cable segments. Thin and thick lines represent 1 h PSD and an average of all available 1 h PSDs. The new low and high noise models, labeled NLNM and NHNM, respectively (Peterson, 1993), are indicated in dashed black lines for broadband data (panels b and d).

HCMR and NESTOR exhibit an additional signature at frequencies of 1–2 Hz. This signal is a local effect, only observed on cable sections inside Methoni Bay, and thus likely related to the seismic response of a sedimentary basin or resonance effects of multiple P-wave reflections in the water column (e.g., Gualtieri et al., 2014). Full analysis of this signal, as recently demonstrated by Spica et al. (2020), is beyond the scope of this manuscript, yet its effect on earthquake ground deformations is further described in Section 5.

Short fiber stretches are deployed on-land between the DAS interrogators' locations and the shorelines. These extra lengths of fiber provide an opportunity to compare the characteristic noise levels on-land and underwater. The PSDs for NESTOR and MEUST, shown in Figure 3 (panels a and c), indicate lower noise levels than those of underwater segments. However, these short on-land segments, do not record any seismic signals, as further discussed in Section 5.

At deeper sections, typically deeper than 2,000 m, the MEUST cable records secondary microseisms, as previously observed by Sladen et al. (2019). These microseisms appear at frequencies of 0.3–2 Hz and are the result of interference between ocean waves traveling in opposite directions (Longuet-Higgins, 1950). As shown by previous studies (e.g., De Caro et al., 2014; Hasselmann, 1963), and similar to gravity waves, secondary microseisms exhibit a frequency decrease with increasing water depth, from 2 Hz at a water depth of 1.4 km to 0.4 Hz at a water depth of 2.4 km, as shown in Figures 2e and 3c. The peak frequency recorded at the end of the MEUST cable (green curve in Figure 3c) matches that observed by the nearby ASEAF OBS (purple curve in Figure 3d), as they are recorded at the same water depth (ASEAF is located 2.47 km beneath sea level).

In addition to natural noise sources, instrumental effects are apparent in Figures 2 and 3. In several frequency bands and distances along the fibers, instrument (interrogator and fiber) related noise dominates the PSDs (Figures 2 and 3), as also seen by the color code in Figure 2. These are slightly higher for the old generation interrogator (used in HCMR and NESTOR) than for the new generation one (used in MEUST), and higher for high frequencies than low frequencies (Fernández-Ruiz et al., 2019). High frequency noise (where strain-rate noise amplitude spectra increase as frequency) levels are characterized by spatial fluctuations along the fibers that are persistent in time and similar for different frequencies. This phenomena is demonstrated in Figure S1, where average PSDs are plotted for a section of MEUST. These small fluctuations (typically lower than 3 dB) are a result of statistical variability of the Cramer-Rao lower bound between adjacent measurements along the fiber (e.g., Costa et al., 2019). The time persistency of these fluctuations are related to the stability of the measurements: a stabilized laser, unperturbed fiber and minute underwater temperature variations. These ideal conditions, typically unavailable on-land, preserve this fluctuation pattern over several days. Even though the amplitude and distance scales of the high-frequency fluctuations could be viewed as similar to those observed for fading (e.g., Gabai & Eyal, 2016), the statistical variability of the Cramer-Rao bound is typically much lower from point to point (typically less than 3 dB over several km, Fernández-Ruiz et al., 2018) and tends to present longer lasting patterns over time (analyzed PSDs are averaged over many hours). Low-frequency noise (where strain-rate noise amplitude spectra are invariant to frequency) is affected by the interrogator's reference updates, which occur every few seconds (Costa et al., 2019), thus a time-persistent pattern is not maintained. Further research is needed to understand and characterize these phenomena over a broader frequency band and for other interrogator types.

Since the used cables were deployed over mostly irregular bathymetry (Figure 1), their ocean-bottom—cable coupling is nonuniform along the cables. This results in gaps in the measurements of coherent signals: gravity waves, microseism signals (Figure 2), and earthquakes (Section 4). In addition, several fiber segments display oscillating patterns, as seen in Figure 2 (e.g., between 12 and 17 km for NESTOR in panel a), which may be related to the fibers' layout, e.g., high tension segments, cables hanging over seafloor valleys. These patterns will require additional research, possibly involving direct inspections of the cable for validation.

Finally, broadband seismometers' noise (panels b and d of Figure 3) are mostly within the limits of the new low/high noise models (NLNM and NHNM) of Peterson (1993). Expected exceptions are the slightly higher low frequency noise, resulting from the proximity of the stations to the Mediterranean basin (e.g., De Caro et al., 2014), and the high amplitude second microseism peak observed for the ASEAF OBS.

The described natural and instrumental noise sources affect earthquake detection and analysis abilities as detailed in following sections. Next, underwater DAS earthquake signals are analyzed and their interactions with observed noise are discussed.

4. DAS Earthquake Signals

Here, the ability to record earthquakes by underwater DAS, and the response of the different cables to transient ground motions are investigated. Then, apparent velocities are inferred and strain-rate measurements are converted to ground motion accelerations and compared with records of adjacent broadband sensors. To this end, several cataloged earthquakes are analyzed: two earthquakes recorded by HCMR, four earthquakes recorded by NESTOR, and two earthquakes recorded by MEUST. Earthquake locations and magnitudes were taken from one of the available catalogs: European-Mediterranean Seismological Center (EMSC), University of Athens, or Géoazur catalogs. The earthquake data is summarized in Table 1 and locations, magnitudes and distances to the interrogators appear in Figure 1. Each figure in this section refers to a specific cable and equivalent figures for the other cables are found in the supplementary.

4.1. Cable Response

Transient deformations are recorded by underwater telecommunication fibers in a nonuniform manner, as recorded earthquake signals vary in amplitude and frequency content along the cable. This is clearly seen in Figure 4 for a magnitude 3.7 earthquake recorded on the HCMR cable (equivalent examples for the NESTOR and MEUST cables are shown in Figures S2 and S3, respectively). The cable's depth profile (panel a), earthquake time series (panel b), amplitude spectra (AS) (panel c) and signal-to-noise-ratio (SNR) (panel d) are plotted as a function of distance along the fiber. These signals are extremely segmented and exhibit amplitude and frequency shifts and jumps (e.g., 5–6 km). While several cable segments record high amplitude seismic signals, others exhibit very weak amplitudes (e.g., 2.5–4 km), or lack seismic signals as seen by the onshore cable segment (0–400 m). Here, and in later parts of the manuscript, SNR is calculated in the frequency domain between 1 and 15 Hz as:

$$\mathrm{SNR} = \sqrt{\frac{\int_{f=1}^{f=15} |\,\mathrm{signal}(f)\,|^2 \, df}{\int_{f=1}^{f=15} |\,\mathrm{noise}(f)\,|^2 \, df}}, \tag{1}$$

where signal*(f)* represents earthquake strain-rate amplitude spectra and noise*(f)* represents strain-rate noise PSD (obtained in Section 3) converted to amplitude spectra. In panel d, SNR are plotted for the displayed earthquake (black curve) and the other analyzed event on the HCMR cable (gray curve). The similarity between SNR patterns along the fiber for different earthquakes (also seen in Figures S2 and S3) indicates that

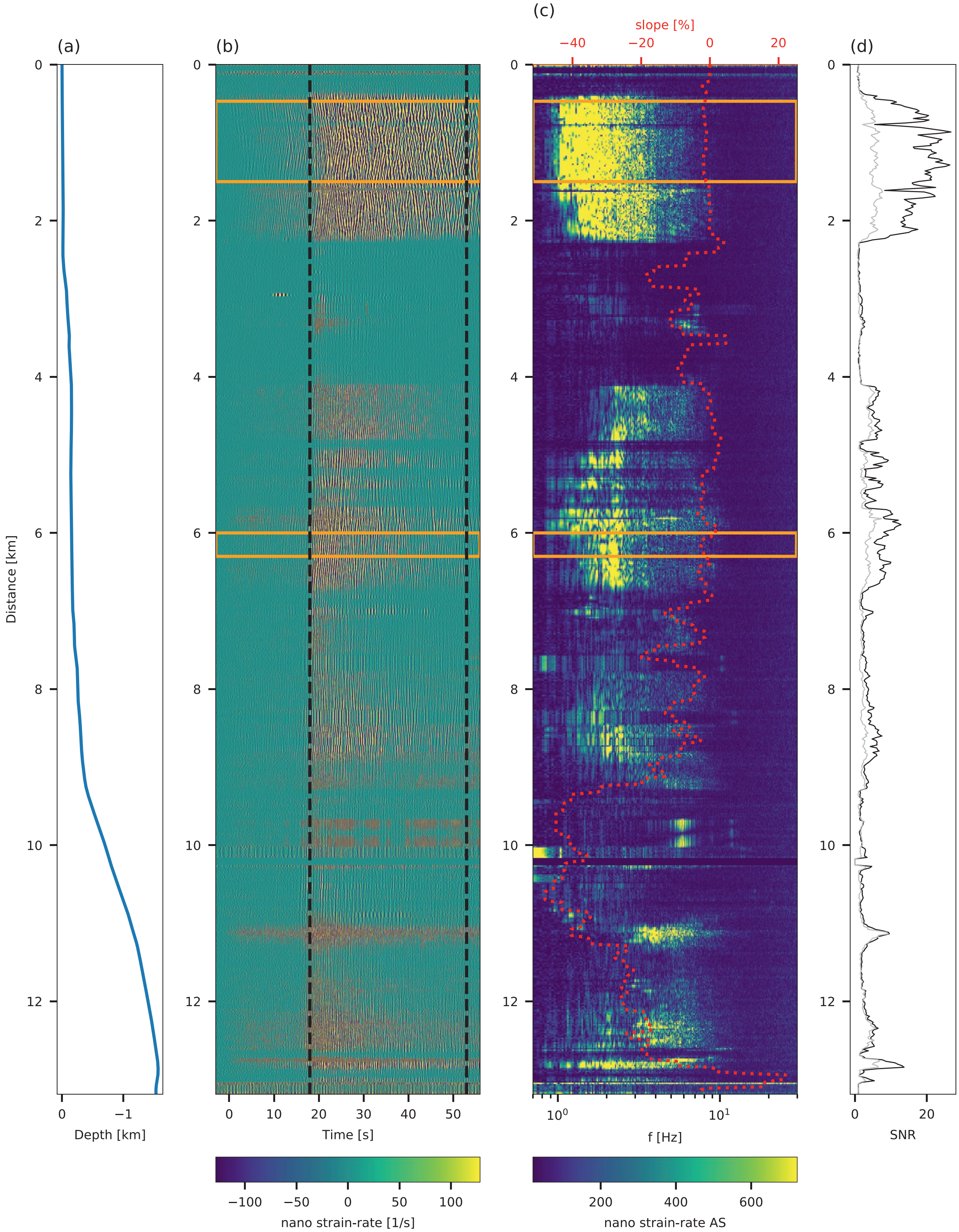

Figure 4. Example of a M3.7 earthquake at approximately 125 km recorded by HCMR. (a) depth profile, (b) earthquake signals, (c) amplitude spectra (AS), and (d) signal to noise ratios along the cable's path (black for this earthquake and gray for the second earthquake recorded by HCMR, see Table 1). Time in panel b is relative to the theoretical P-wave arrival at the cable position of 0 km (closest point to the earthquake epicenter). S-wave spectra in (c) are computed in the interval indicated by dashed black lines in (b). The slope of the cable is plotted in red in panel c. Sections that are used in subsequent analysis are indicted by orange rectangles.

this cable specific property may be used to quantify ground-cable coupling as well as ground deformation amplifications along the cable.

Sections where signals are weak typically correspond to irregular bathymetry, while high amplitude seismic deformations are measured by fiber segments deployed on flat or smooth bathymetry. This correlation is evident when comparing the recorded signals' quality with the bathymetry (Figure 4a) and slope (red dotted curve in Figure 4c) along the cable. For example, shallow sections of HCMR and NESTOR record high-energy signals (Figures 4 and S2): these segments are deployed inside Methoni Bay, a sedimentary basin characterized by flat bathymetry and low velocities (Section 4.2). In contrast, sections outside Methoni Bay (toward the ocean bottom) exhibit irregular bathymetry and low amplitude signals. Thus, flat or smooth bathymetry, characterized by high amplitude recordings suggests the presence of sediments, which control amplification and slowness. In contrast, irregular bathymetry and low amplitude recordings may suggest uneven coupling and/or lack of sediments. It is also possible that the observed response is related to the buried/unburied character of the cable, yet it can only be tested using direct observations of the cables' deployment, which are currently unavailable.

The SNR pattern (Figures 4d and S2d) smoothly increase and decrease when entering and exiting Methoni Bay (0.3–2.3 km in Figure 4d and 2.3–2.8 km in Figure 4d). This observation suggests the presence of a sedimentary basin: as sediment thickness increases from the edges toward the middle of the basin, so does ground motion amplification (e.g., Gualtieri et al., 2015). This SNR pattern may thus be indicative of cable segments traversing sedimentary basins.

In-spite of the often unfavorable ocean-bottom—cable recording quality, several cable segments record sufficiently uniform signals for seismic analysis and specifically, apparent velocity estimation. Two such sections are identified for each cable, indicated by orange rectangles in panels b and c of Figures 4, S2, and S3. Their signals are analyzed in the following sections.

4.2. Strain-Rate to Ground Motions Conversion

To further investigate the response of underwater DAS to transient ground deformations, DAS signals are compared to the ground motion measurements recorded by nearby seismometers. The ability to convert DAS records to ground motions was investigated and demonstrated by several previous studies (e.g., Daley et al., 2016; Lindsey et al., 2020; Paitz et al., 2020; Wang et al., 2018). To convert strain-rate records to ground motions, phase velocities need to be determined. Here, we use the waves' apparent phase velocities along the fiber, assuming the signal is dominated by a single plane wave:

$$\dot{\epsilon}_{xx} = \frac{\partial U_x}{\partial t \partial x} = \frac{\partial V_x}{\partial x} = \frac{\partial V_x}{\partial t}\frac{\partial t}{\partial x} = A_x \frac{1}{C_x}, \tag{2}$$

where $\dot{\epsilon}_{xx}$, U_x, V_x, A_x, and C_x are the strain-rate, ground displacements, ground velocities, ground accelerations, and apparent phase velocity along the fiber (x direction), respectively. Equation 2 has been frequently used for this purpose by various previous studies (e.g., Lellouch et al., 2019; Lindsey et al., 2020; Wang et al., 2018). The relation between the phase velocity C and the apparent phase velocity is: $C_x = C / \cos\theta$, where θ is the angle between the wave's propagation direction and the fiber. The apparent velocity is expected to change along the cable due to local conditions, sedimentary cover, seismic wave velocities and propagation direction with respect to the cable's orientation. Here, apparent velocities are estimated via frequency-wavenumber (f-k) analysis, and DAS strain-rate measurements are converted to ground accelerations in the frequency-domain. DAS converted spectra are then compared to broadband seismometer spectra.

Apparent velocities are reliably estimated using homogeneous DAS signals recorded on sufficiently long cable segments. Apparent phase velocities are defined as f / ν where f and ν are the temporal and spatial frequencies, respectively. This analysis is performed on the segments identified in the previous section (orange rectangles in panels b and c of Figures 4, S2, and S3). Example f-k plots are shown in Figure 5 (top panels) for four earthquakes recorded on the NESTOR cable between 0.35 and 1.5 km from the interrogator, on a section deployed in Methoni Bay. Similar f-k plots for all cable segments are shown in Figures S4–S8.

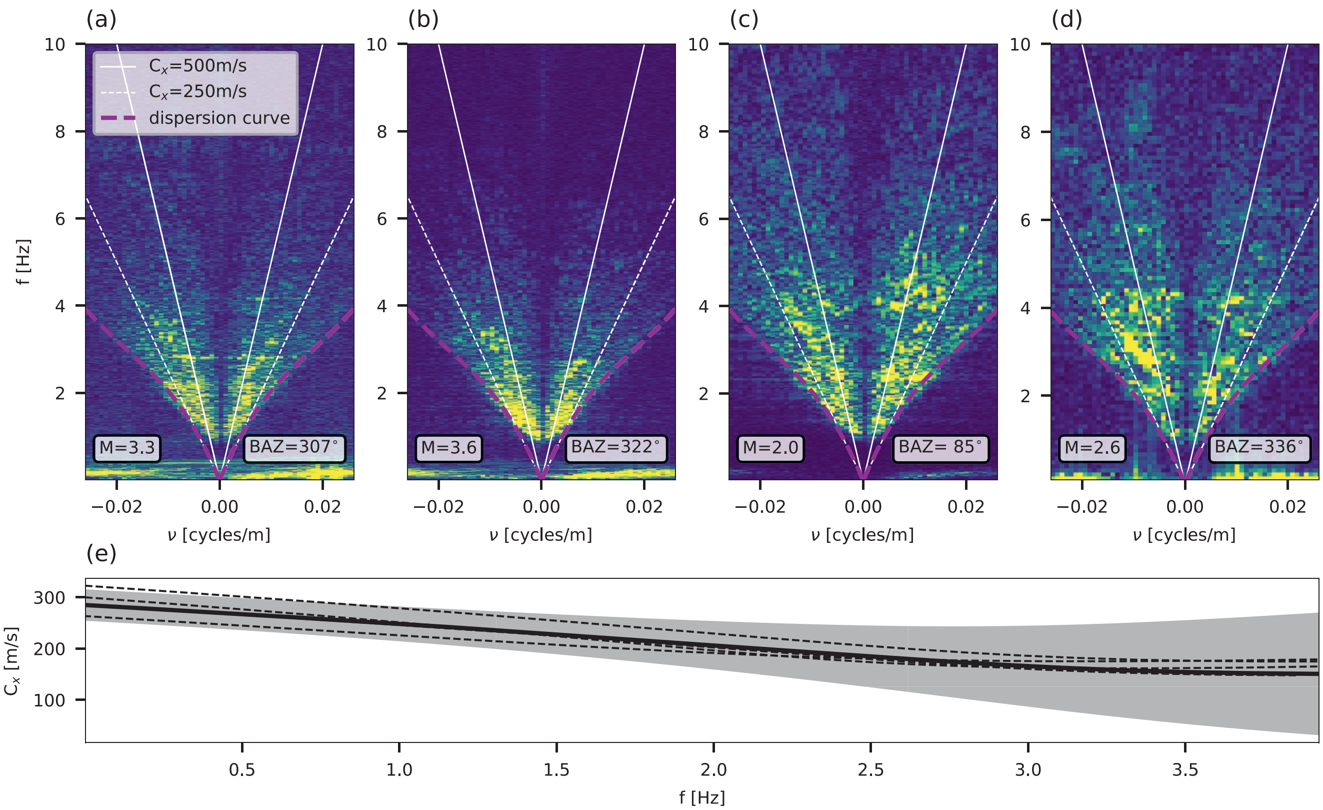

Figure 5. Panels (a–d): Examples of *f-k* plot for four earthquakes on a segment of the NESTOR cable from 0.35 to 1.5 km. Earthquake magnitudes and backazimuths (BAZ) values are indicated in each panel. The average cable orientation in this segment is 159° ± 12°. The empirical dispersion curve is indicated in magenta in panels (a–d) and in panel (e). White lines correspond to nondispersive phase velocities of 500 m/s (solid line) and 250 m/s (dotted line). Panel (e) shows the apparent velocity as a function of frequency obtained for all earthquakes at once (solid black curve) and for each event individually (dashed black curves). Shaded gray area indicates one standard deviation to solid black curve's fit.

The observed low apparent velocities, generally symmetric *f-k* plots (as previously reported by Lindsey et al. [2019], Sladen et al. [2019], and Williams et al. [2019]), and similarity between different earthquakes with different backazimuths (BAZ) (receiver-to-source azimuth), suggest that underwater DAS signals are dominated by Scholte-waves propagating in a broad range of horizontal directions.

Scholte waves are a result of body-wave scattering, and their polarization is radial and vertical, similar to that of Rayleigh waves (Biot, 1952; Scholte, 1947). Since the analyzed fiber segments are installed on typically flat bathymetry, the radial polarization dominates DAS measurements. Strain-rate measurements of waves propagating at an angle θ relative to the fiber's axis are modulated by a $\cos^2\theta$ (e.g., Kuvshinov et al., 2016; Mateeva et al., 2014), significantly reducing the amplitude of waves closer to normal incidence. Thus, it is expected that the highest amplitude waves recorded by DAS are those traveling along the fiber, with $C_x = C$ (note that generally $C_x \geq C$), i.e., the lowest apparent velocity in the *f-k* plot (top panels of Figure 5). Thus, the phase velocity used for DAS to ground motion conversion is the lowest apparent velocity, represented by the purple curve in Figure 5 which separates the low and high energy regions in the *f-k* plots. Apparent velocities as a function of frequency, deduced from the curves in Figure 5, are shown in panel e. The dispersive nature of the waves further supports the conclusion that these are Scholte-waves.

Apparent velocities (purple curve in Figure 5) are obtained for all analyzed events per cable segment. That *f-k* plots are symmetric and similar for different earthquakes recorded by the same segment suggests similar propagation characteristics, as expected for scattered waves: their propagation and velocity is dictated by local heterogeneities and velocity model. Thus, the same apparent velocity is used for all analyzed earthquakes regardless of source and backazimuth variations.

10.1029/2020JB020925

For each event in a specific cable segment, the boundary between the low and high energy regions (top panels of Figure 5) is determined per frequency by a simple amplitude threshold condition. Then, these $f - \nu$ combinations are averaged per spatial frequency ν for all available events, and fitted with a third degree polynomial passing through $f = \nu = 0$ to obtain the purple curve in Figure 5. Apparent velocity errors, represented by the gray region in Figure 5e, indicate one standard deviation computed using the polynomial fit. For comparison, dispersion curves were obtained independently for each earthquake following the same procedure (dashed curves in Figure 5e). The velocity error suggested by the polynomial fit is larger than the standard deviation of the four different event specific apparent velocities (dashed curves in Figure 5e). The latter are small: 18.9 and 8.6 m/s at 1 and 4 Hz, respectively, further justifying the use of a single dispersion curve for all earthquakes. For several cable segments, the spatial resolution is inadequate (short cable segments on HCMR and NESTOR, Figures S4 and S5) and *f-k* plots were fitted with a simpler linear equation passing $f = \nu = 0$, corresponding to nondispersive waves. The dispersion curves in Figure 5e (as well as Figures S6–S8) represents a frequency-band limited view of propagation velocities. Since dispersion curves typically plateau at higher frequencies, in subsequent analysis higher frequency phase velocities are approximated as the velocity of the highest resolvable frequency (e.g., 3.9 Hz in Figure 5e). This conservative estimate may change should higher frequency observations be available. In the following section, broadband sensors' acceleration records are converted to strain-rate using the empirical apparent velocities obtained per cable segment. Converted broadband spectra are then compared to DAS spectra.

4.3. DAS and Broadband Comparison

Broadband earthquake acceleration spectra are converted to strain-rate and compared with DAS measurements. The conversion was done using the same dispersion curve (Figure 6) or single apparent velocity (Figure 7) for each cable segment. Here, broadband spectra were corrected for hypocentral distance to match with the different DAS cable segments. Figures 6 and 7 show DAS strain-rate time series along the cable (left panels), S-wave spectra along the cable (middle panels), and a comparison between DAS and broadband converted strain-rate spectra (right panels) for four earthquakes recorded on the NESTOR cable. In the right panels, DAS earthquake spectra and mean noise (obtained in Section 3) for each measurement point along the cable segment are plotted as thin black and red curves, respectively, while stacked signal and noise are plotted as thick black and red curves, respectively. These earthquake spectra are resampled in the same manner as noise spectra (McNamara & Buland, 2004) for comparability.

Broadband converted acceleration spectra agree with DAS strain-rate spectra when the latter are corrected for site effects. Excellent agreement is observed between DAS and broadband converted spectra for the two closest events in Figure 6 (M2 at 49 km and a depth of 2 km, and M2.6 at 63 km and a depth of 9 km), while the agreement for farther earthquakes is less favorable (M3.3 at 130 km and a depth of 11 km, and M3.6 at 149 km and a depth of 7 km), possibly a result of different propagation effects. In contrast, DAS spectra in Figure 7, recorded in Methoni Bay, are rich in low frequencies and poor in high frequencies. Similar behavior is observed for HCMR, when comparing signals recorded outside (Figures S5) and inside (Figures S6) Methoni Bay, as well as for different MEUST sections (Figures S7 and S8). The amplification observed for MEUST (Figure S8) is related to the secondary microseismic peak (Figure 2), while that observed in Methoni Bay is related to the presence of a low velocity (Figures 5 and S6) basin, as suggested by the noise peak at 1–2 Hz (Figure 2). The stronger attenuation inside the basin may be modeled by a decaying exponential term in the form: $\exp\left(-\pi\Delta\kappa f\right)$ (Anderson & Hough, 1984), where $\Delta\kappa$ indicates additional attenuation. Imposing such attenuation on the observed broadband spectra (dashed curves in the right panels of Figure 7) results in good agreement between high frequency DAS and broadband spectra.

To quantify the amplification and attenuation observed by HCMR and NESTOR, the ratio between DAS spectra recorded inside and outside Methoni Bay is inspected in Figure 8. The seemingly tapered edges of these curves represent the signals' amplitudes falling below background noise levels, thus, only frequencies between ~1 and ~15 Hz (depending on SNR) should be considered. Earthquakes recorded inside Methoni Bay show significant amplification of up to a factor of 10 at frequencies of 1–2 Hz, and stronger atten-

10.1029/2020JB020925

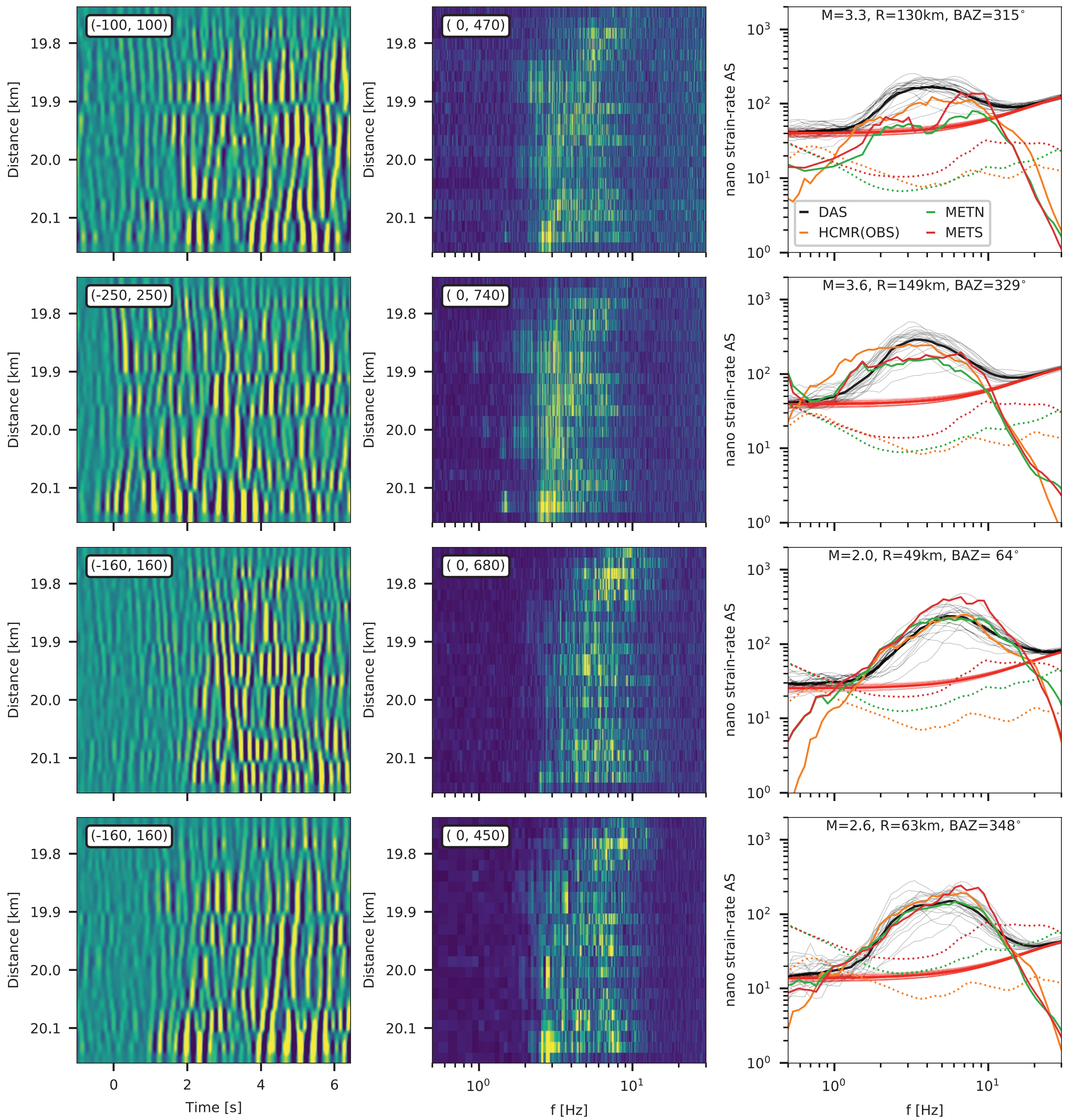

Figure 6. Spectral analysis for four earthquakes recorded by NESTOR between 19.7 and 20.2 km from the interrogator, between 3.1 and 3.3 km depth. Left panels: time series, middle panels: amplitude spectra (in linear scale), right panels: strain-rate spectra and converted broadband seismometer spectra. Plotted time series (left) were filtered between 1 and 5 Hz. Time in the left panels is relative to the start of the analyzed interval. In the left and middle columns, the minimum and maximum values plotted in each panel are indicated in parentheses in the top left corner. In the right panels, DAS earthquake and noise spectra for each measurement location along the fiber are indicated by thin black and red curves, respectively, while averages are indicated by thick lines. Noise amplitude spectra were calculated from noise PSDs (Section 3) using a duration equal to the earthquake time window. Solid green and dark red curves correspond to records from on-land seismometers near the on-land end of the fiber, while the solid orange curve corresponds to the record of an ocean-bottom seismometers (OBS) installed at the end of the HCMR cable. Dotted curves show seismometers' noise amplitude spectra, calculated from noise PSDs and converted to strain-rate. Note that DAS and seismometer PSD were converted to amplitude spectra using different durations.

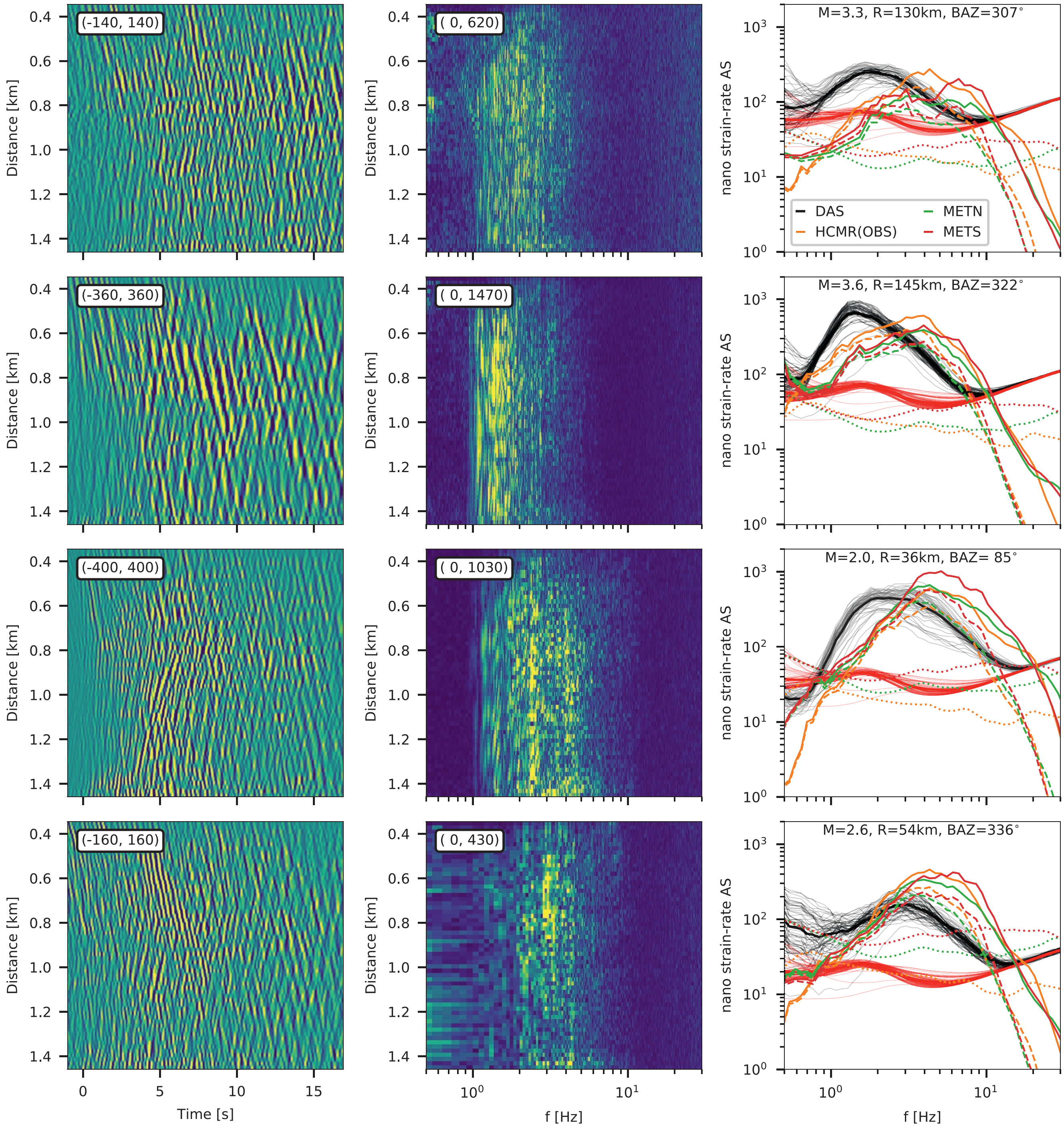

Figure 7. As in Figure 6 for a section between 0.35 and 1.5 km from the interrogator, between 3 and 18 m depth. Dashed curves indicate strain-rate converted broadband spectra subject to additional attenuation ($\Delta\kappa = 0.04$ s).

uation in the 2–20 Hz band compared with signals recorded outside the bay. This behavior is indicative of sedimentary basins, which are generally characterized by low seismic velocities (e.g., Courboulex et al., 2020; Pratt et al., 2003).

In the next section, we quantify the ability to detect seismic signals using underwater DAS and compare it to that of broadband seismometers.

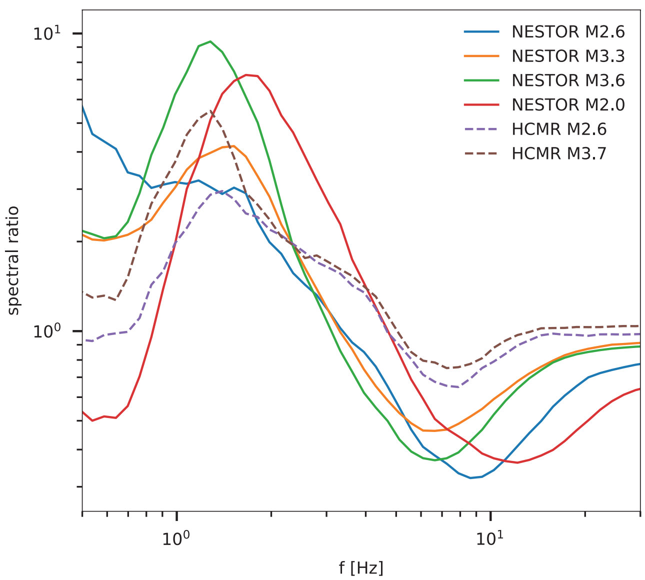

Figure 8. Methoni Bay amplification. Spectral ratios of distance corrected DAS spectra for events recorded in and out of Methoni Bay: thick black curves in right panels of Figure 7 (averaged earthquake AS recorded between 0.35 and 1.5 km along NESTOR) and S6 (averaged earthquake AS recorded between 0.5 and 1.5 km along HCMR) divided by thick black curves in right panels of Figure 6 (averaged earthquake AS recorded between 19.7 and 20.2 km along NESTOR) and S5 (averaged earthquake AS recorded between 6 and 6.3 km along HCMR), respectively.

5. Implications for DAS Detection Capabilities

The results presented in the previous section, in particular the conversion between strain and ground motions, based on apparent velocities estimated on each cable segment, are used here to analyze underwater DAS single-channel signal-to-noise ratio (SNR) capabilities, and compare them to those of broadband seismometers. For a valid comparison, this analysis treats DAS signals as independent channels. The spatial coherency between waveforms recorded along the optical fiber, a unique strength of DAS facilitating the implementation of high-performance array detection methods (e.g., Lindsey et al., 2017; Rost & Thomas, 2002), is expected to enhance earthquake detection capabilities, but is not exploited here. In that sense, our analysis is a conservative estimate of the performance of seafloor DAS relative to conventional seismometers. In this section, only the new generation interrogator is considered, since it better represents state-of-the-art DAS capabilities. Because the earthquakes we have recorded are typically observed at $f > 1$ Hz (Figures 5–7), this analysis is limited to this frequency band.

5.1. S-wave Detection on Horizontal Underwater Fibers

DAS detection capabilities are analyzed by considering an earthquake model, DAS noise (obtained in Section 3), and the apparent velocities (obtained in Section 4.2). Earthquake acceleration spectra are simulated using the omega-squared model (Brune, 1970; Madariaga, 1976) describing far field body-wave radiation, and subject to high frequency attenuation (Anderson & Hough, 1984). This model is found to be in good agreement with observed DAS and broadband spectra (not shown). The model, and associated parameter tuning, are described in the supplementary. Horizontally deployed fibers exhibit higher sensitivity to S-waves than P-waves, a function of the phase's polarization with respect to the fiber (e.g., Ajo-Franklin et al., 2019; Kuvshinov, 2016; Mateeva et al., 2014; Papp et al., 2017; Yu et al., 2018). Owing to the lower velocities and higher amplitudes of S-waves, they display higher strain amplitudes, compared with P-waves (Section 6). Thus, only S-waves are considered in the following analysis. To determine DAS detection thresholds, i.e., signal to noise ratios in a certain frequency-band, for specific cable segments, DAS strain-rate are converted to acceleration noise PSDs (Equation 2) and compared to the earthquake model.

Using the apparent velocities for the slow Scholte-waves (e.g., Figure 5), detection thresholds are found to be similar for DAS and broadband seismometers. Strain rate noise PSDs were converted to acceleration for the MEUST cable at 12.4 and 30.2 km from the interrogator, constituting phase velocity dependent DAS detection thresholds. Figure 9 shows these DAS detection thresholds along with those of adjacent on-land (POSAS) and ocean-bottom (ASEAF) broadband seismometers. Detection thresholds are compared to ground motion accelerations for earthquakes of magnitudes 1 and 2 at a hypocentral distance of 50 km. These thresholds indicate great similarity between the detection capabilities of DAS (solid curves in Figure 9) and nearby broadband OBS (dotted orange curve in Figure 9) for the same underwater environment and noise conditions (Section 3).

The ability to detect a seismic signal using DAS greatly depends on the apparent velocity: at similar acceleration amplitudes, the slower the wave, the higher its strain-rate values (Equation 2). This is illustrated in Figures 10 and 11, by modeling DAS and broadband SNR values for different magnitude earthquakes between 1 and 15 Hz. We use the SNR definition in Equation 1 where here signal*(f)* represents modeled earthquake accelerations amplitude spectra (m/s), and noise*(f)* represents strain-rate noise PSD converted to amplitude spectra (unitless) and multiplied by $C_x(f)$, the frequency dependent apparent phase velocity (m/s). Signals are simulated using the same earthquake model used in Figure 9 at a hypocentral distance of 50 km (Figure 10) and for various distances (Figure 11). Acceleration spectra noise thresholds are obtained for MEUST at 12.4 km from the interrogator using different nondispersive apparent velocities. The

10.1029/2020JB020925

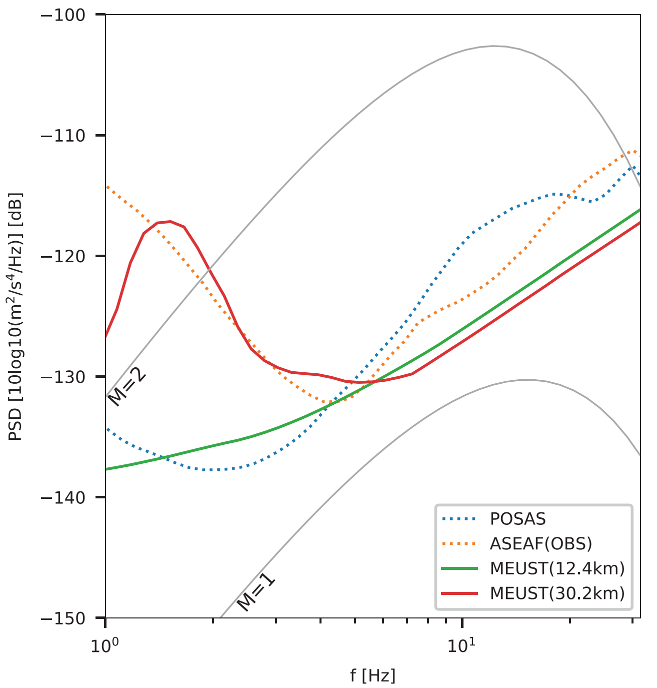

Figure 9. DAS and broadband noise spectra compared to theoretical S-wave spectra. Magnitudes 1 and 2 at distances of 50 km and $\kappa = 0.04$ s are indicated by solid gray curves. Representative DAS noise curves are shown for MEUST at 12.4 (solid green) and 30.2 km (solid red). Noise curves for broadband seismic stations on-land POSAS and underwater ASEAF, located near MEUST, are indicated by dotted blue and orange curves, respectively.

apparent velocity is used to convert DAS strain-rate to acceleration detection threshold, while modeled earthquake acceleration spectra do not account for apparent velocities (supplementary materials). This analysis indicates that for a specific phase velocity, DAS and broadband SNR are equivalent (green and blue curves in Figure 10), while slower and faster waves produce higher and lower SNR on DAS, respectively. In Figure 11, SNR = 1 curves are plotted for different magnitude-distance combinations, constituting detection thresholds for various apparent velocities: waves to the right of each curve are detected while those to the left are not. This plot may be used to evaluate the ability to reliably use S-waves for seismic monitoring for different magnitudes and distances. Phase velocity uncertainties can be incorporated in this analysis: since SNR is scaled by $1 / C_x$ (Equation 1), for example, a 24% relative error in the apparent velocity estimates (as identified for a frequency of 2 Hz in the dispersion curve in Figure 5e), will cause an equivalent relative error in SNR estimate.

The presented analysis indicates that for a given earthquake, and depending on the ground motion amplitudes, slow phases (e.g., scattered and surface waves) may be detected, while fast phases (e.g., body waves) may not. For instance, plotting DAS earthquake (black) and noise (red) spectra at two different HCMR cable segments (Figure 12), we can observe either low velocity (240 m/s) high energy strain-rate signals (from 6 to 6.3 km, Figure S5), or high velocity (1,690 m/s) low energy strain-rate signals (from 2.3 to 2.85 km, Figure S9). Both slow and fast waves are detected for the M3.7 earthquake (panel a), while only slow waves are detected for the M2.6 earthquake (panel b). Broadband converted strain-rate spectra of the HCMR OBS using the obtained apparent velocities (orange and green curves) further show that the fast waves of the M2.6 earthquake are below DAS noise levels (green curve in panel b). Since both analyzed earthquakes display similar backazimuths and distances, and thus similar propagation characteristics, the apparent velocity obtained for the M3.7 earthquake (Figure S9) is used to convert the broadband spectra of the M2.6 earthquake to strain-rate (orange dashed curve in Figure 12b).

In this analysis, on-land cable segments did not measure any earthquake ground deformations. The longest on-land section is that of MEUST, deployed for 1.6 km: from the interrogator's position to the coast, along a two-lane motorway. This segment displays noise levels similar to those recorded at deeper underwater segments (Figure 3c), and clearly records vehicles driving along the road. That no seismic signals are recorded on this segment is interpreted as a result of high apparent velocities, in agreement with previous studies, which show that on-land Rayleigh waves are faster than ocean bottom Scholte-waves (e.g., Biot, 1952; Kruiver et al., 2010; Park et al., 2005; Scholte, 1947). This observation suggests that DAS detection capabilities are enhanced for underwater fibers compared with those installed on-land. Since unlike DAS records, ground motion amplitudes (and thus broadband detection capabilities) are invariant to the wave's velocity, OBS are not expected to outperform on-land seismometers.

5.2. P-wave Detection on Horizontal Underwater Fibers and Implications for EEW

That fast waves may not be detected by DAS has significant implications for several seismological tasks that rely on the information carried by fast direct body-waves. These objectives include the determination of earthquake location and source parameters, both crucial for seismic monitoring and, in particular, for EEW. Using the P-waves is particularly advantageous for EEW since waiting for the S-waves comes at the cost of delaying alert issuance. However, the detection capabilities of fast, low amplitude, P-waves on horizontal optical fibers is hindered by both the high apparent velocities and near-vertical incident angles; vertically incident P-waves induce transverse deformations on a horizontal cable, while fibers are mostly sensitive to longitudinal deformations. This issue of broadside sensitivity has been demonstrated and

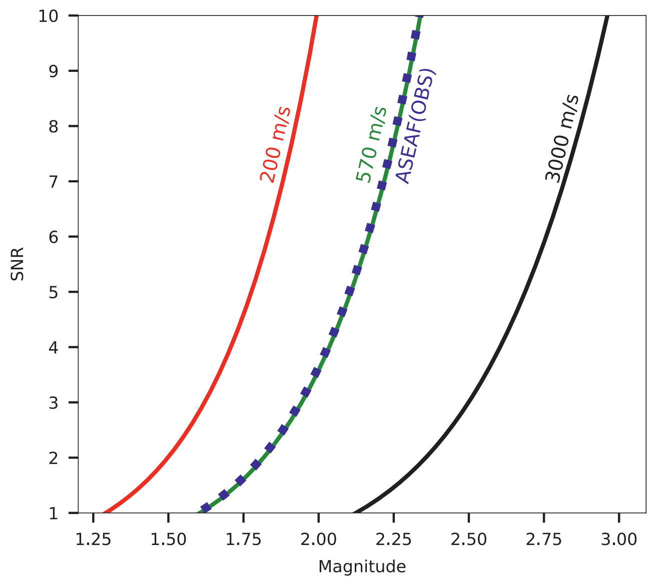

Figure 10. S-wave signal-to-noise-ratio (SNR) calculated between 1 and 15 Hz for ground accelerations as a function of magnitude. Earthquake spectra were simulated at a hypocentral distance of 50 km and $\kappa = 0.04$ s. DAS noise, calculated on MEUST at 12.4 km from the interrogator, was converted to ground accelerations using several nondispersive apparent velocities. SNR for ASEAF (the OBS at the end of MEUST) are indicated by the dotted blue curve. SNR for DAS with apparent velocities of 200, 570, and 3,000 m/s are indicated by solid red, green and black curves, respectively.

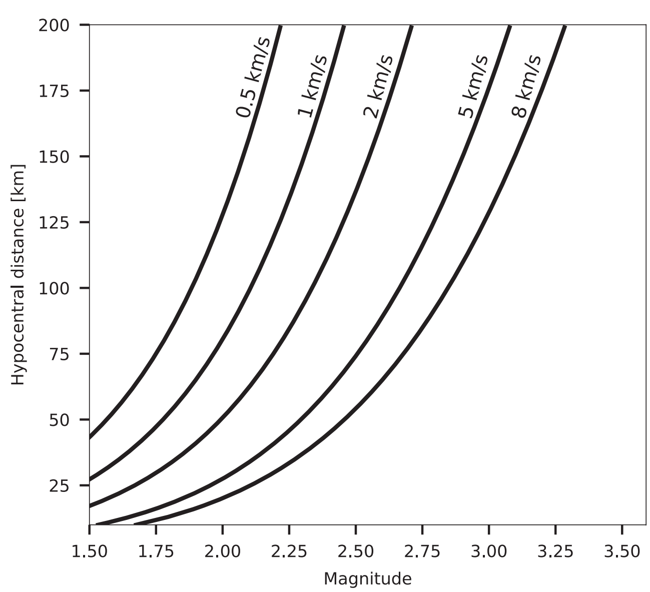

Figure 11. S-wave detection thresholds (SNR = 1), calculated between 1 and 15 Hz, for ground accelerations at different apparent velocities. Earthquake spectra and noise were simulated as in Figure 10 for various magnitudes and hypocentral distances. For each apparent velocity, S-waves at magnitudes-distances to the right of each curve are above noise level.

studied in both lab experiments (e.g., Papp et al., 2017), and seismic experiments (e.g., Mateeva et al., 2014). The response of a fiber optic cable to waves propagating at an angle θ with respect to the fiber is modulated by $\cos^2\theta$. Though signals do not vanish completely at $\theta = 90°$ (Kuvshinov et al., 2016; Mateeva et al., 2014; Papp et al., 2017), they have much smaller amplitude and will hardly be detected.

In practice, P-waves are detected since underwater cables follow the bathymetry and are thus not strictly horizontal (panels c–e of Figure 1), and since incidence angles, especially for scattered P-waves, would typically be smaller than 90°. Even for small magnitudes at large distances, as those analyzed, scattered P-waves are observed for several earthquakes (e.g., in Methoni Bay, Figure 4). Thus, for earthquakes relevant for EEW, i.e., medium to big magnitudes (M>~4) at close distances (R<~150 km) (e.g., Lior & Ziv, 2020), whose ground motion accelerations are expected to be at least two orders of magnitude higher than those recorded here (e.g., Lior & Ziv, 2020) (Figures 6 and 7), P-waves will be detected. This indicates that underwater telecommunication cables may be reliably used for P-wave detection and thus for EEW, improving alert times for underwater earthquakes. In-depth quantitative analysis of this issue requires further research, beyond the scope of this manuscript, and additional high amplitude earthquake observations.

If P-waves cannot be reliably analyzed, the use of S-waves for both tasks is still expected to yield robust estimates, at the cost of time delays. For closely recorded earthquakes, relevant for EEW, these delays are expected to be small, since S-waves follow P-waves by approximately R/8 s, where R is the hypocentral distance in km (e.g., Lior & Ziv, 2018).

6. Conclusions

This study presents a comprehensive analysis of underwater DAS measurements, addressing both noise and earthquake recordings along three underwater dark fibers in the Mediterranean Sea. This analysis presents various noise sources including surface gravity waves, secondary microseisms and local basin resonance. The effect of these noise sources, as well as ocean-bottom—cable coupling, on measured ground deformations is demonstrated using several small ($M_L < 3.7$) well recorded regional earthquakes. Finally, the ability to detect seismic phases using underwater DAS is discussed for both P- and S-waves.

The bathymetric profiles along the different cables' are found to be sufficiently valid for this study's purposes. Surface gravity waves and secondary microseisms frequency variations qualitatively agree with the bathymetry (Section 3), bathymetry variations are found to be well correlated with earthquake recording quality (Section 4.1), and DAS and seismometers' spectra agree following hypocentral distance corrections (Section 4.3).

A significant correlation is observed between irregular bathymetry and unfavorable DAS measurements (Figures 4, S2, and S3). Flat or smooth bathymetric slopes typically correspond to sediment accumulating regions, while irregular bathymetry prevents sediment deposition. The former may create conditions for better coupling and even burial of underwater cables by sediment deposition, while the latter will prevent cable burial and may even represent regions of erosion. Sedimentary basins are

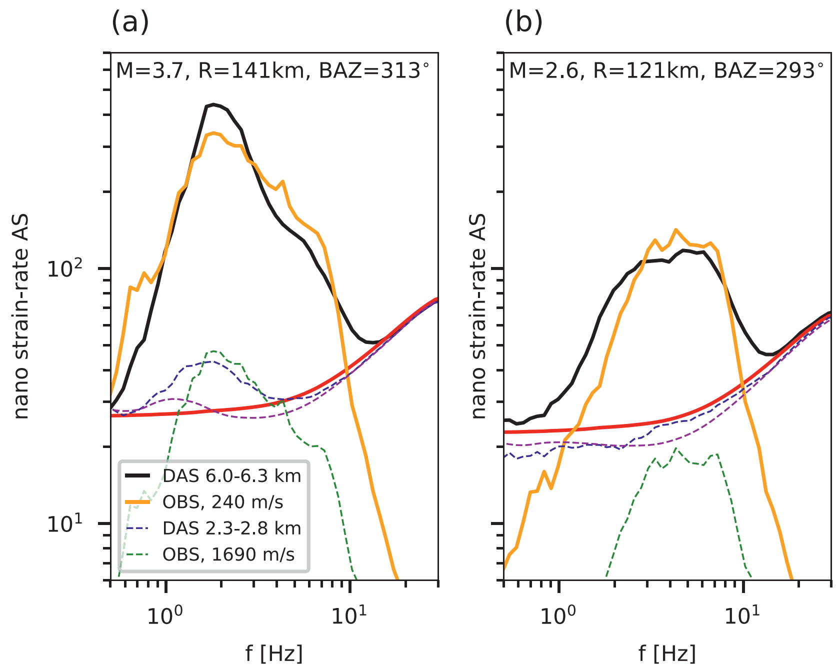

Figure 12. Comparison between earthquakes recorded by two cable segments on HCMR. Solid curves and dashed curves represent the analysis for recordings at 6–6.3 and 2.3–2.8 km along the cable, respectively. Black and blue curves correspond to stacked DAS spectra, red and magenta curves correspond to stacked DAS noise, and orange and green curves correspond to broadband converted strain-rate. Broadband spectra were converted to strain-rate using different apparent velocities as noted by the legend. Magnitudes, distances and BAZ values are indicated in the top of each panel.

characterized by low seismic velocities (e.g., Figure 5) and excellent coupling (e.g., Figure 4), while regions that lack sedimentary cover are characterized by higher seismic velocities (e.g., Figure S9). In addition, deploying underwater fibers over irregular bathymetry may result in uneven coupling and even cable segments hanging in the water column. It is concluded that the bathymetry dictates the measurement quality, by modulating phase velocities and ground-cable coupling.

Frequency-wavenumber analysis indicates that underwater DAS earthquake records are dominated by slow scattered dispersive Scholte-waves. Broadband earthquake spectra are converted to strain-rate using apparent velocities obtained via *f-k* analysis. Since this analysis was done for scattered Scholte-waves, a single apparent velocity or dispersion curve was used for all earthquakes recorded by the same cable segment. However, when analyzing direct phases, apparent velocities will differ depending on the propagation path and wave-fiber incidence angle, requiring an earthquake specific analysis. Excellent agreement is found between DAS and converted broadband spectra, when the latter is corrected for local amplification and attenuation effects. A local sedimentary basin is identified using both coherent noise and earthquake signals, and is shown to amplify and attenuate low and high frequency seismic signals, respectively.

Detection capabilities are enhanced by lower velocity seafloor sediments. DAS detection capabilities are found to be strongly correlated with apparent velocities: for the same ground motion amplitudes, slow and fast waves induce high and low energy DAS strain records, respectively. DAS and broadband detection abilities were found to be similar for the recorded earthquake phases (Figure 9). That on-land sections did not record the analyzed earthquakes is attributed to higher on-land velocities, a phenomenon that suggests that DAS detection capabilities are enhanced underwater. Our conservative analysis does not use the spatial coherence of DAS data, a powerful property that may be used to associate and denoise coherent signals. Thus, the ability to analyze earthquakes using underwater DAS is expected to be superior to that of broadband sensors, even for equivalent SNR.

The results demonstrate the great potential of underwater DAS for seismic monitoring and for providing EEW using standard underwater telecommunication cables. The latter will greatly enhance hazard mitigation capabilities, increase warning times for underwater earthquakes, and potentially save many lives.

Data Availability Statement

DAS data were acquired using a first generation Febus A1 interrogator and an Aragon Photonics hDAS interrogator. Broadband seismometer data were acquired by Géoazur except for OBS records: data for the ASEAF, POSAN, and POSAS stations were downloaded from RESIF (http://seismology.resif.fr/, last accessed May 2020). The MEUST infrastructure is financed with the support of the CNRSIN2P3, the Region Sud, France (CPER the State (DRRT), and the Europe (FEDER). The fiber optic DAS earthquake recordings used to generate Figures 2–7, S2, and S3, and the curves plotted in Figure 3 are available in the following OSF repository: https://osf.io/4bjph/.

Acknowledgments
We thank the editor, Yehuda Ben-Zion, for his work, and Lucia Gualtieri and an anonymous reviewer for their very constructive remarks. This work and I.L. were supported by the SEAFOOD project, funded in part by grant ANR-17-CE04-0007 of the French Agence Nationale de la Recherche. Part of the project was also supported by Université Côte d'Azur IDEX program UCA[JEDI] ANR-15-IDEX-0001 and the Doeblin Federation (FR2800 CNRS). H.F.M. acknowledge financial support from the Spanish MICINN under contract no. IJCI-2017-33856.

References

Aggouras, G., Anassontzis, E., Ball, A. E., Bourlis, G., Chinowsky, W., Fahrun, E., et al. (2005). Operation and performance of the NESTOR test detector. *Nuclear Instruments and Methods in Physics Research Section A: Accelerators, Spectrometers, Detectors and Associated Equipment*, *552*(3), 420–439. https://doi.org/10.1016/j.nima.2005.06.083

Ajo-Franklin, J. B., Dou, S., Lindsey, N. J., Monga, I., Tracy, C., Robertson, M., et al. (2019). Distributed acoustic sensing using dark fiber for near-surface characterization and broadband seismic event detection. *Scientific Reports*, *9*(1), 1328. https://doi.org/10.1038/s41598-018-36675-8

Allen, R. M., & Melgar, D. (2019). Earthquake early warning: advances, scientific challenges, and societal needs. *Annual Review of Earth and Planetary Sciences*, *47*(1), 361–388. https://doi.org/10.1146/annurev-earth-053018-060457

Anassontzis, E., & Koske, P. (2003). Deep-sea station connected by cable to the shore. *Sea Technology*, *44*(7), 10–14. Retrieved from https://inspirehep.net/literature/641751

Anderson, J. G., & Hough, S. E. (1984). A model for the shape of the Fourier amplitude spectrum of acceleration at high frequencies. *Bulletin of the Seismological Society of America*, *74*(5), 1969–1993.

Biot, M. A. (1952). The interaction of Rayleigh and Stoneley waves in the ocean bottom. *Bulletin of the Seismological Society of America*, *42*(1), 81–93.

Brune, J. N. (1970). Tectonic stress and the spectra of seismic shear waves from earthquakes. *Journal of Geophysical Research*, *75*(26), 4997–5009. https://doi.org/10.1029/JB075i026p04997

Costa, L., Martins, H. F., Martin-Lopez, S., Fernandez-Ruiz, M. R., & Gonzalez-Herraez, M. (2019). Fully distributed optical fiber strain sensor with 10^{-12} $\epsilon/\sqrt{\mathrm{Hz}}$ sensitivity. *Journal of Lightwave Technology*, *37*(18), 4487–4495. https://doi.org/10.1109/JLT.2019.2904560

Courboulex, F., Mercerat, E. D., Deschamps, A., Migeon, S., Baques, M., Larroque, C., et al. (2020). Strong site effect revealed by a new broadband seismometer on the Continental Shelf Offshore Nice Airport (Southeastern France). *Pure and Applied Geophysics*, *177*(7), 3205–3224. https://doi.org/10.1007/s00024-019-02408-9

Daley, T. M., Miller, D. E., Dodds, K., Cook, P., & Freifeld, B. M. (2016). Field testing of modular borehole monitoring with simultaneous distributed acoustic sensing and geophone vertical seismic profiles at Citronelle, Alabama: Field testing of MBM. *Geophysical Prospecting*, *64*(5), 1318–1334. https://doi.org/10.1111/1365-2478.12324

De Caro, M., Monna, S., Frugoni, F., Beranzoli, L., & Favali, P. (2014). Seafloor seismic noise at Central Eastern Mediterranean Sites. *Seismological Research Letters*, *85*(5), 1019–1033. https://doi.org/10.1785/0220130203

Fernández-Ruiz, M. R., Costa, L., & Martins, F. H. (2019). Distributed acoustic sensing using chirped-pulse phase-sensitive OTDR technology. *Sensors*, *19*(20), 4368. https://doi.org/10.3390/s19204368

Fernández-Ruiz, M. R., Martins, H. F., Costa, L., Martin-Lopez, L., & Gonzalez-Herraez, M. (2018). Steady-sensitivity distributed acoustic sensors. *36*(23), 5690–5696. https://doi.org/10.1109/JLT.2018.2877849

Finetti, I. (1982). Structure, stratigraphy and evolution of Central Mediterranean. *Bollettino di Geofisica Teorica ed Applicata*, *24*(96), 247–312.

Gabai, H., & Eyal, A. (2016). On the sensitivity of distributed acoustic sensing. *Optics Letters*, *41*(24), 5648. https://doi.org/10.1364/OL.41.005648

Gualtieri, L., Stutzmann, E., Capdeville, Y., Farra, V., Mangeney, A., & Morelli, A. (2015). On the shaping factors of the secondary microseismic wavefield. *Journal of Geophysical Research: Solid Earth*, *120*(9), 6241–6262. https://doi.org/10.1002/2015JB012157

Gualtieri, L., Stutzmann, E., Farra, V., Capdeville, Y., Schimmel, M., Ardhuin, F., & Morelli, A. (2014). Modelling the ocean site effect on seismic noise body waves. *Geophysical Journal International*, *197*(2), 1096–1106. https://doi.org/10.1093/gji/ggu042

Hasselmann, K. (1963). A statistical analysis of the generation of microseisms. *Reviews of Geophysics*, *1*(2), 177. https://doi.org/10.1029/RG001i002p00177

Jousset, P., Reinsch, T., Ryberg, T., Blanck, H., Clarke, A., Aghayev, R., et al. (2018). Dynamic strain determination using fibre-optic cables allows imaging of seismological and structural features. *Nature Communications*, *9*(1), 2509. https://doi.org/10.1038/s41467-018-04860-y

Kruiver, P. P, Deák, A., & El Allouche, N. (2010). Extraction of geotechnical properties from Scholte waves in underwater environments. *1st International Conference on Frontiers in Shallow Subsurface Technology* (pp. 29–32). Houten, The Netherlands: EAGE. Retrieved from https://www.earthdoc.org/detail.php?pubid=37456

Kuvshinov, B. N. (2016). Interaction of helically wound fibre-optic cables with plane seismic waves: Interaction of fibre-optic cables. *Geophysical Prospecting*, *64*(3), 671–688. https://doi.org/10.1111/1365-2478.12303

Lamare, P. (2016). The MEUST deep sea infrastructure in the Toulon site. *EPJ Web of Conferences*, *116*, 09001. https://doi.org/10.1051/epjconf/201611609001

Lellouch, A., Yuan, S., Spica, Z., Biondi, B., & Ellsworth, W. L. (2019). Seismic velocity estimation using passive downhole distributed acoustic sensing records: examples from the san andreas fault observatory at depth. *Journal of Geophysical Research: Solid Earth*, *124*(7), 6931–6948. https://doi.org/10.1029/2019JB017533

Lindsey, N. J., Dawe, T. C., & Ajo-Franklin, J. B. (2019). Illuminating seafloor faults and ocean dynamics with dark fiber distributed acoustic sensing. *Science*, *366*(6469), 1103–1107. https://doi.org/10.1126/science.aay5881

Lindsey, N. J., Martin, E. R., Dreger, D. S., Freifeld, B., Cole, S., James, S. R., et al. (2017). Fiber-optic network observations of earthquake wavefields. *Geophysical Research Letters*, *44*(23), 11792–11799. https://doi.org/10.1002/2017GL075722

Lindsey, N. J., Rademacher, H., & Ajo-Franklin, J. B. (2020). On the broadband instrument response of fiber-optic DAS arrays. *Journal of Geophysical Research: Solid Earth*, *125*(2), e2019JB018145. https://doi.org/10.1029/2019JB018145

Lior, I., & Ziv, A. (2018). The relation between ground motion, earthquake source parameters, and attenuation: Implications for source parameter inversion and ground motion prediction equations. *Journal of Geophysical Research: Solid Earth*, *123*(7), 5886–5901. https://doi.org/10.1029/2018JB015504

Lior, I., & Ziv, A. (2020). Generic source parameter determination and ground-motion prediction for earthquake early warning. *Bulletin of the Seismological Society of America*, *110*(1), 345–356. https://doi.org/10.1785/0120190140

Longuet-Higgins, M. S. (1950). A theory of the origin of microseisms. *Philosophical Transactions of the Royal Society of London. Series A, Mathematical and Physical Sciences*, *243*(857), 1–35.

Madariaga, R. (1976). Dynamics of an expanding circular fault. *Bulletin of the Seismological Society of America*, *66*(3), 639–666.

Mateeva, A., Lopez, J., Potters, H., Mestayer, J., Cox, B., Kiyashchenko, D., et al. (2014). Distributed acoustic sensing for reservoir monitoring with vertical seismic profiling: Distributed acoustic sensing (DAS) for reservoir monitoring with VSP. *Geophysical Prospecting*, *62*(4), 679–692. https://doi.org/10.1111/1365-2478.12116

McNamara, D. E., & Buland, R. P. (2004). Ambient noise levels in the continental United States. *Bulletin of the Seismological Society of America*, *94*(4), 1517–1527. https://doi.org/10.1785/012003001

Paitz, P., Edme, P., Gräff, D., Walter, F., Doetsch, J., Chalari, A., et al. (2020). Empirical investigations of the instrument response for distributed acoustic sensing (DAS) across 17 octaves. *Bulletin of the Seismological Society of America*, *111*(1), 1–10. https://doi.org/10.1785/0120200185

Papp, B., Donno, D., Martin, J. E., & Hartog, A. H. (2017). A study of the geophysical response of distributed fibre optic acoustic sensors through laboratory-scale experiments: Geophysical response of fibre optic sensors. *Geophysical Prospecting*, *65*(5), 1186–1204. https://doi.org/10.1111/1365-2478.12471

Park, C. B., Miller, R. D., Xia, J., Ivanov, J., Sonnichsen, G. V., Hunter, J. A., et al. (2005). Underwater MASW to evaluate stiffness of water-bottom sediments. *The Leading Edge*, *24*(7), 724–728. https://doi.org/10.1190/1.1993267

Pastor-Graells, J., Martins, H. F., Garcia-Ruiz, A., Martin-Lopez, S., & Gonzalez-Herraez, M. (2016). Single-shot distributed temperature and strain tracking using direct detection phase-sensitive OTDR with chirped pulses. *Optics Express*, *24*(12), 13121. https://doi.org/10.1364/OE.24.013121

Peterson, J. R. (1993). *Observations and modeling of seismic background noise* (Report No. 93–322; Open-File Report). USGS Publications Warehouse. https://doi.org/10.3133/ofr93322

Pratt, T. L. (2003). Amplification of seismic waves by the seattle basin, washington state. *Bulletin of the Seismological Society of America*, *93*(2), 533–545. https://doi.org/10.1785/0120010292

Rost, S., & Thomas, C. (2002). Array seismology: Methods and applications. *Reviews of Geophysics*, *40*(3), 2-1–2-27. https://doi.org/10.1029/2000RG000100

Scholte, J. G. (1947). The range of existence of Rayleigh and Stoneley waves. *Geophysical Journal International*, *5*(5), 120–126. https://doi.org/10.1111/j.1365-246X.1947.tb00347.x

Sladen, A., Rivet, D., Ampuero, J. P., De Barros, L., Hello, Y., Calbris, G., & Lamare, P. (2019). Distributed sensing of earthquakes and ocean-solid Earth interactions on seafloor telecom cables. *Nature Communications*, *10*(1), 1–8. https://doi.org/10.1038/s41467-019-13793-z

Spica, Z. J., Nishida, K., Akuhara, T., Pétrélis, F., Shinohara, M., & Yamada, T. (2020). Marine Sediment Characterized by Ocean-Bottom Fiber-Optic Seismology. *Geophysical Research Letters*, *47*(16), https://doi.org/10.1029/2020GL088360

Vallée, M., Ampuero, J. P., Juhel, K., Bernard, P., Montagner, J.-P., & Barsuglia, M. (2017). Observations and modeling of the elastogravity signals preceding direct seismic waves. *Science*, *358*(6367), 1164–1168. https://doi.org/10.1126/science.aao0746

Wang, H. F., Zeng, X., Miller, D. E., Fratta, D., Feigl, K. L., Thurber, C. H., & Mellors, R. J. (2018). Ground motion response to an M_L 4.3 earthquake using co-located distributed acoustic sensing and seismometer arrays. *Geophysical Journal International*, *213*(3), 2020–2036. https://doi.org/10.1093/gji/ggy102

Webb, S. C., & Crawford, W. C. (2010). Shallow-water broadband OBS seismology. *Bulletin of the Seismological Society of America*, *100*(4), 1770–1778. https://doi.org/10.1785/0120090203

Williams, E. F., Fernández-Ruiz, M. R., Magalhaes, R., Vanthillo, R., Zhan, Z., González-Herráez, M., & Martins, H. F. (2019). Distributed sensing of microseisms and teleseisms with submarine dark fibers. *Nature Communications*, *10*(1), 5778. https://doi.org/10.1038/s41467-019-13262-7

Yu, C., Zhan, Z., Lindsey, N. J., Ajo-Franklin, J. B., & Robertson, M. (2019). The potential of DAS in teleseismic studies: Insights from the goldstone experiment. *Geophysical Research Letters*, *46*(3), 1320–1328. https://doi.org/10.1029/2018GL081195

Zhan, Z. (2020). Distributed acoustic sensing turns fiber-optic cables into sensitive seismic antennas. *Seismological Research Letters*, *91*(1), 1–15. https://doi.org/10.1785/0220190112